

# Jerky motion of dislocations in high-entropy alloys: The linkage between local Peierls stress fluctuations and dislocation mobility

Daniel Utt<sup>1,\*</sup>, Subin Lee<sup>2,3,\*</sup>, Alexander Stukowski<sup>1</sup>,  
Sang Ho Oh<sup>4</sup>, Gerhard Dehm<sup>2</sup>, Karsten Albe<sup>1</sup>

<sup>1</sup> Fachgebiet Materialmodellierung, Institut für Materialwissenschaft, Technische Universität Darmstadt, Darmstadt, Germany

<sup>2</sup> Structure and Nano-/ Micromechanics of Materials, Max-Planck-Institut für Eisenforschung, Düsseldorf, Germany

<sup>3</sup> Center for Integrated Nanostructure Physics, Institute for Basic Science, Suwon, Republic of Korea

<sup>4</sup> Department of Energy Science, Sungkyunkwan University, Suwon, Republic of Korea  
\* [utt@mm.tu-darmstadt.de](mailto:utt@mm.tu-darmstadt.de), [s.lee@mpie.de](mailto:s.lee@mpie.de)

## Abstract

Dislocation lines in concentrated medium and high-entropy alloys are pinned during glide resulting in jerky motion. While solute interaction with dislocations is well understood in conventional alloys, the origin and action of individual pinning points in concentrated random alloys is a matter of debate. Here we report transmission electron microscope investigations combined with atomistic computer simulations and identify the local Peierls stress for each atom in the dislocation glide plane as a spatial descriptor for dislocation pinning sites. We show that the density and magnitude of pinning sites correlates well with the dislocation mobility. By comparing different Ni based alloys we find that the non-linear interaction between Co and Cr leads to a pronounced increase in pinning point density and strength. Finally, we find that the insertion of artificial short-range order does not change the pinning point landscape.

## 1 Introduction

Several high and medium-entropy alloys (HEA/MEA) outperform mechanical properties of conventional alloys, while some even combine exclusive property combinations such as high strength and high ductility - even down to cryogenic temperatures [1, 2, 3]. Meanwhile it is well established that configurational entropy of most HEA is not outperforming enthalpic interactions [4, 5], and HEAs are better referred to as multi-principle element alloys. The strong enthalpy contributions are documented by local chemical ordering [6, 5, 7], phase decomposition [8, 9], and tunable stacking fault energies [10].

The origin of high strength of HEA and MEA is controversially discussed in the community [11, 12, 5, 13]. Curtin and coworkers [14] developed a model predicting flow stresses for solid solution strengthening in multi-principle element alloys solely based on misfit volumes and elasticity. In their recent study they exclude that SRO is required to match the yield stresses found in experiments for the CrMnFeCoNi family including the ternary MEA CrCoNi [11]. Several research groups [15, 16, 17] performed detailed transmission electron microscopy

(TEM) and/or atom probe tomography studies on CrMnFeCoNi and related alloys without resolving any trace of short-range order (SRO). Recently, R. Zhang et al. observed, however, weak reflections at  $1/2(111)$  for the CrCoNi MEA in energy-filtered transmission electron diffraction indicating local chemical ordering [12]; similarly F.X. Zhang *et al.* identified SRO by X-ray absorption fine structure (EXAFS) enhanced by density functional theory [18]. Upon annealing fine precipitates evolved from the SRO in CrCoNi supporting their view that local chemical ordering is a crucial factor in the strength of multi-principle element alloys [12]. SRO is indirectly supported by trains of dislocations which traveled along the same path as displayed in TEM images of deformed CrCoNi, CrFeCoNi, CrMnFeCoNi alloys [19]. Dislocation trains sweeping over an area of SRO are typically expected to destroy pinning sites as repeated slip by subsequent dislocations randomizes any local chemical order. The destruction of pinning sites is however, not observed in our recent in-situ TEM results revealing jerky dislocation glide by repeated pinning and depinning along the lines of consecutive dislocations [17].

If SRO is not the underlying mechanism, a differ-

ent interpretation is pending [20]. The unexpected range of (complex) stacking fault energies observed by atomistic simulations and TEM studies could be an alternative scenario explaining why dislocations experience pinning sites along their lines leading to increased lattice resistance [21, 5]. The resulting wavy dislocation lines have been observed for different HEA/MEA in experiments [21, 22, 5, 17] and atomistic simulations [21, 14, 23, 24, 7, 25]. Li *et al.* argue that the wide range of stacking fault energy (SFE) causes peaks in the energy landscape where locally lattice friction becomes enhanced [5]. As a consequence dislocation segments need to unzip from the local barriers while gliding. Such a mechanism would only exist in MEA/HEA, but not in conventional dilute solid solutions.

In this study we investigate the repeated local pinning along subsequent dislocations in the face-centered cubic (FCC) CoCrFeMnNi HEA by combining in-situ TEM and atomistic simulations. The in-situ TEM studies reveal wavy dislocation lines and their jagged motion even under an applied tensile strain. These observations are reproduced in atomistic computer simulations without the need for SRO. The underlying mechanism is directly linked to locally varying fluctuations in Peierls barriers, which lead to dislocation pinning points in chemically complex alloys, and show their relation to the critical stress needed for moving a dislocation line.

## 2 Results

We first start with the experimental analysis of the structure and glide motion of dislocations in CoCrFeMnNi HEA by in-situ TEM tensile testing (Fig. 1 and Supplementary Video 1). Uniaxial tensile load is applied to the Cu grid which transfers stress to the HEA thin foil prepared by FIB lift-out (Fig. 1 (a)). The loading direction and the viewing direction (or electron beam direction) are  $[21\bar{1}]$  and  $[113]$ , respectively. Under  $[21\bar{1}]$  zone axis, three (111) slip planes are inclined with respect to the viewing direction except (*a*) plane in Thompson notation. Due to limited thickness of the thin foil, dislocations glide on one of inclined slip planes are connected to top and bottom surface of the foil (Fig. 1). At the very outermost surface, there is a FIB-affected layer, which is either partly amorphous and/or contains dislocation loops [26]. During deformation, dislocations bow out under the local shear stress toward their glide direction (Fig. 1 (b, c)).

In Fig. 1 (c) representative snapshots are presented showing the glide motion of Shockley partial dislocations separated by stacking faults appearing as dark bands. All images are processed data in order to have a better contrast of dislocations (details

in Method section). While gliding, dislocations advance through kink-pair-like glide mechanism. For example, for the case of the dislocation, *D*, indicated by black arrow, only the upper part of the dislocation line (blue arrow) moves forward. With some delay, the bottom part (green arrow) follows. The jerky motion can be more clearly seen by comparing the dislocation position over time (Fig. 1 (d)). The positions are extracted by using Gaussian and ridge detection image filters. As described above, a small dislocation segment propagates by forming small humps, while the rest hardly moves. This glide motion by continuous pinning-unpinning is observed for most dislocations, and could be the reason for the high shear stress required for dislocation glide in HEAs [17].

Local chemical ordering or clustering might affect the pinning and depinning of dislocations, however, in this alloy, we could not resolve them even with state-of-the-art chemical analysis by STEM energy-dispersive X-ray spectroscopy (EDS) and atom probe tomography [17]. We can also exclude experimental artifacts, such as FIB damages or surface oxide, since both are located at the outer-most surface of the TEM sample and have a thickness of 5-10 nm (Fig. 1(b)) [27]. Therefore, the jerky motion in the middle part of the dislocations, which is placed near the center of the TEM foil should not be affected by the external artifacts.

Fig. 1(e) shows the evolution of the first Shockley partial dislocation emitted from a surface crack in an atomistic simulation. Colored dislocation lines show the growth of the dislocation loop in 1 ps increments. Analogous to the TEM observations an inherent waviness of the dislocation can be seen. As all atoms in the simulated sample are distributed randomly (Supplementary Fig. 5), we see that even in the absence of SRO localized dislocation pinning can be observed. This supports the notion, that the random chemical fluctuations in the HEA are sufficient to pin the dislocation line. In the following we will investigate the equimolar CoCrFeMnNi HEA using the LAMMPS software [28] and a classical interatomic potential [29] to determine the origin of these nano-scale dislocation pinning points.

The classical Peierls model of dislocation glide states that the stress required to move a dislocation is proportional to the maximum slope in the energy path connecting two neighboring stable states. For pure metals this energy path may be approximated by a sinusoid and the so-called Peierls stress can be calculated analytically. In dilute solid solutions the local energy function is changed around each solute and therefore the local stresses required for dislocation glide change. Nevertheless, the local Peierls stress can still be calculated from the slope of said energy curve [30, 31].

The general-stacking-fault (GSF) energy surface

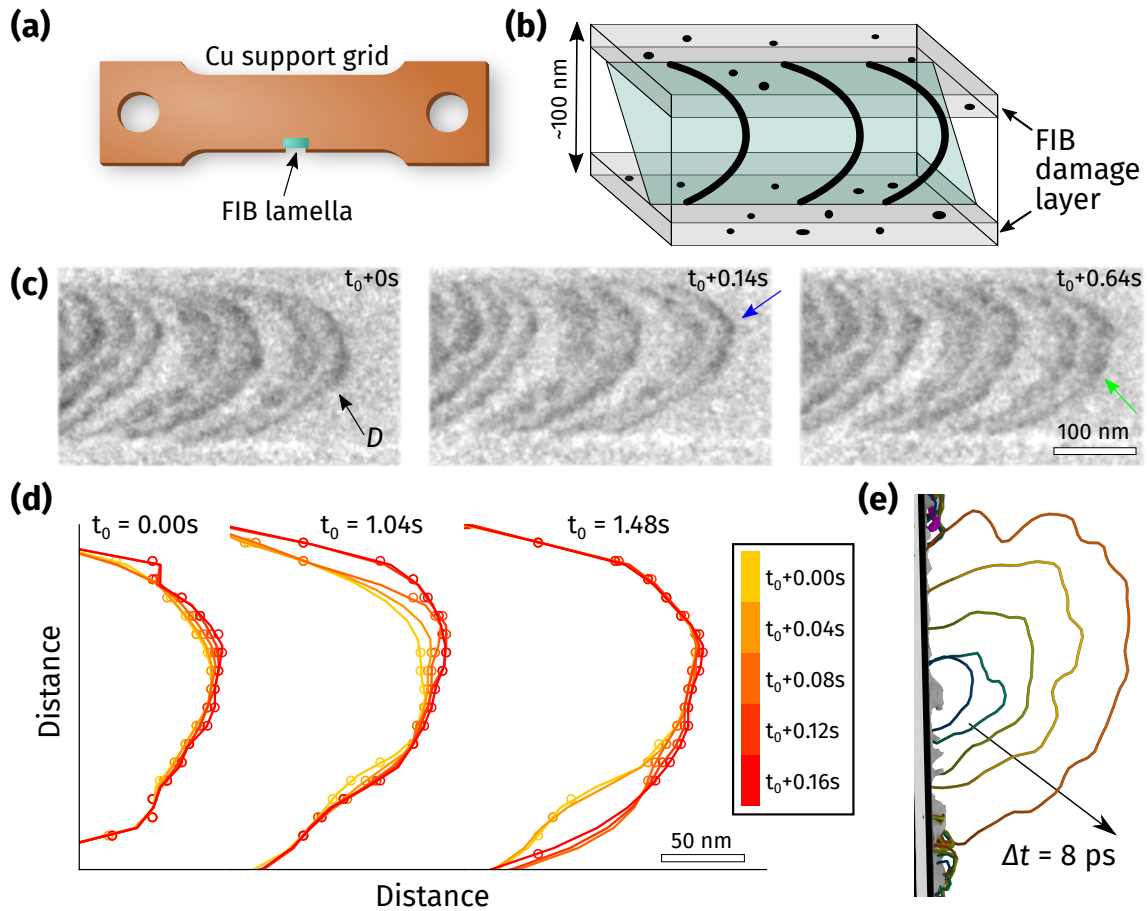


Figure 1: Jerky glide motion of dislocations in Cantor alloy during in-situ TEM straining. (a) Schematic illustration of the experimental setup. FIB lamella is lifted-out to custom-made Cu straining grid. (b) Schematic drawing show the slip plane and dislocation array in a thin TEM sample. The glide plane is inclined and the ends of dislocations are attached to top and bottom surfaces of the lamella. FIB damage is only at the very near surface, so that the center part of dislocations should not be affected from them. (c) Snapshots of in-situ TEM straining movie. Dislocations show jerky glide motion. Dislocations continuously form small humps while propagating as indicated by blue and green arrows. (d) Three sets of the trace of the dislocation,  $D$ , over time extracted from TEM images by image processing. The wavy shape is due to local pinning causing jerky glide motion. (e) Growth of a Shockley partial emitted from a surface notch under applied tensile load in the computer simulation. Similar to the experiment, a wavy dislocation line can be seen.

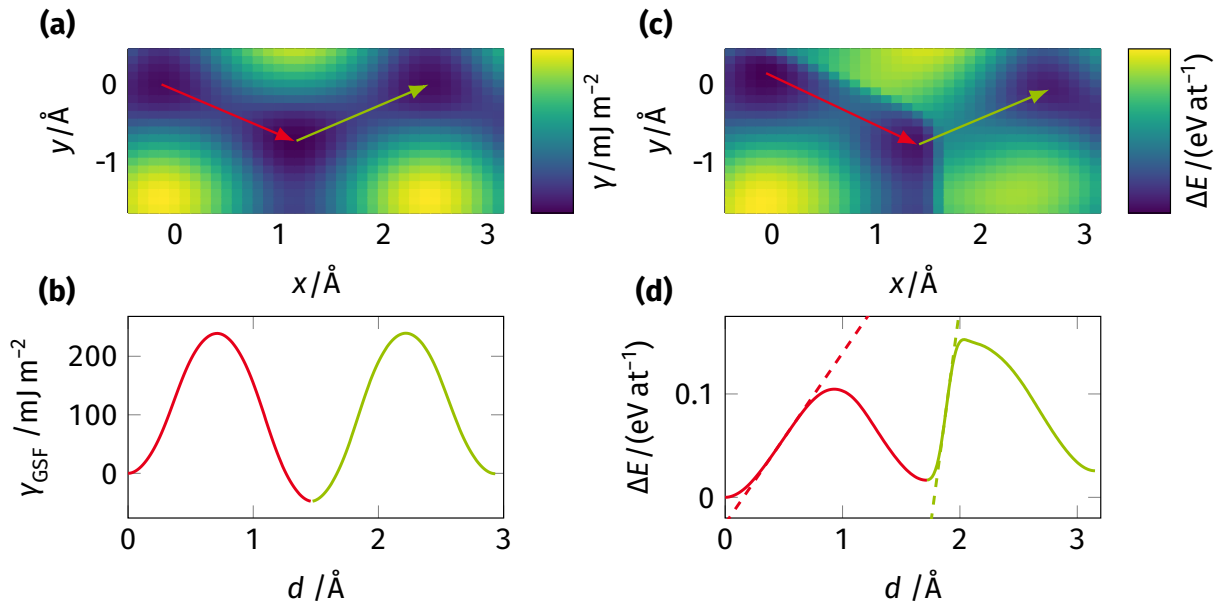


Figure 2: Stacking fault energy averaged for the CoCrFeMnNi sample (a-b) and an example for the localized stacking fault energy calculated for a single atom (c-d). (a) Generalized stacking fault energy (GSF) curve along the leading (red) and trailing (green) partial dislocation’s displacement. GSF surface (b) with arrow indicating the minimum energy path connecting two stable FCC sites via a HCP site. (c) Minimum energy path connecting the local minima of the corresponding GSF surface shown in (d). (c & d) are shown as an example for a single Co atom in the GSF plane. Dashed lines indicate the maximum slope (in units of force)  $F_{\text{GSF}}$ .

is the energy profile for the rigid displacement of two crystal planes [32, 33, 34] and it is often taken as stand-in for the Peierls energy. Conventionally, the GSF energy surface is calculated as an average over the whole GSF plane. For example, Fig. 2 (a) gives the averaged GSF energy surface for the HEA sample. The energy profile along the displacement of leading (marked by red) and trailing (marked by green) partial dislocations shows symmetric shape as shown in Fig. 2 (b). However, in the case of HEAs, we expect the GSF energy surface to strongly vary based on the local atomic arrangement. Therefore, the Peierls stress becomes a local quantity which has to be calculated for each atom. Fig. 2 (c) and (d) give an example of such a local GSF curve. Compared to a monoatomic metal there are two notable differences in local GSF curve of HEAs; Firstly, the energy path for leading and trailing partials are not symmetric as there are pronounced changes in the local chemical environment after the first displacement. The maximum slope of the GSF curve also becomes asymmetric which corresponds to the local critical force  $F_{\text{GSF}}$  required to move a dislocation segment. Secondly, the three local minima are shifted compared to the perfect FCC positions due to spatial variations in the equilibrium bond length [35].

In order to see the effect of the local fluctuations in the GSF energy surface and thereby in the local  $F_{\text{GSF}}$  a constant shear force is applied to the

dislocation. To minimize the effect of thermal fluctuations the temperature is set to 2 K.

Fig. 3 (a-c) show a 3D representation of the local  $F_{\text{GSF}}$ , and thereby also the local dislocation pinning point landscape. Superimposed is the dislocation line at different times as it travels through the crystal. The dislocation is pinned on the highest obstacle and strongly bows out under the applied load (b). After the dislocation has passed over a given area, the atoms are shuffled and the dislocation obstacle landscape has changed for following dislocations.

Fig. 3 (d) shows the position of the leading partial dislocation under applied shear load over a 20 ps interval in 0.25 ps increments. Positions, where multiple line segments are close to each other, correspond to positions where the dislocation line is locally pinned while wider line spacing indicate faster dislocation glide. Gray circles highlight positions of increased  $F_{\text{GSF}}$ , which we propose to lead to a locally increased dislocation line pinning.

To effectively correlate  $F_{\text{GSF}}$  with the dislocation position during dislocation glide we collect the leading partial’s dislocation positions on a  $3 \times 3 \text{ \AA}^2$  binning grid. The dislocation position is extracted every 10 fs and the every bin that is touched by the dislocation line has its count incremented by 1. This leading partial occupation  $C_{\text{leading}}$  is shown in (b). Brighter regions in the plot correspond to regions of longer dwelling time for the dislocation and

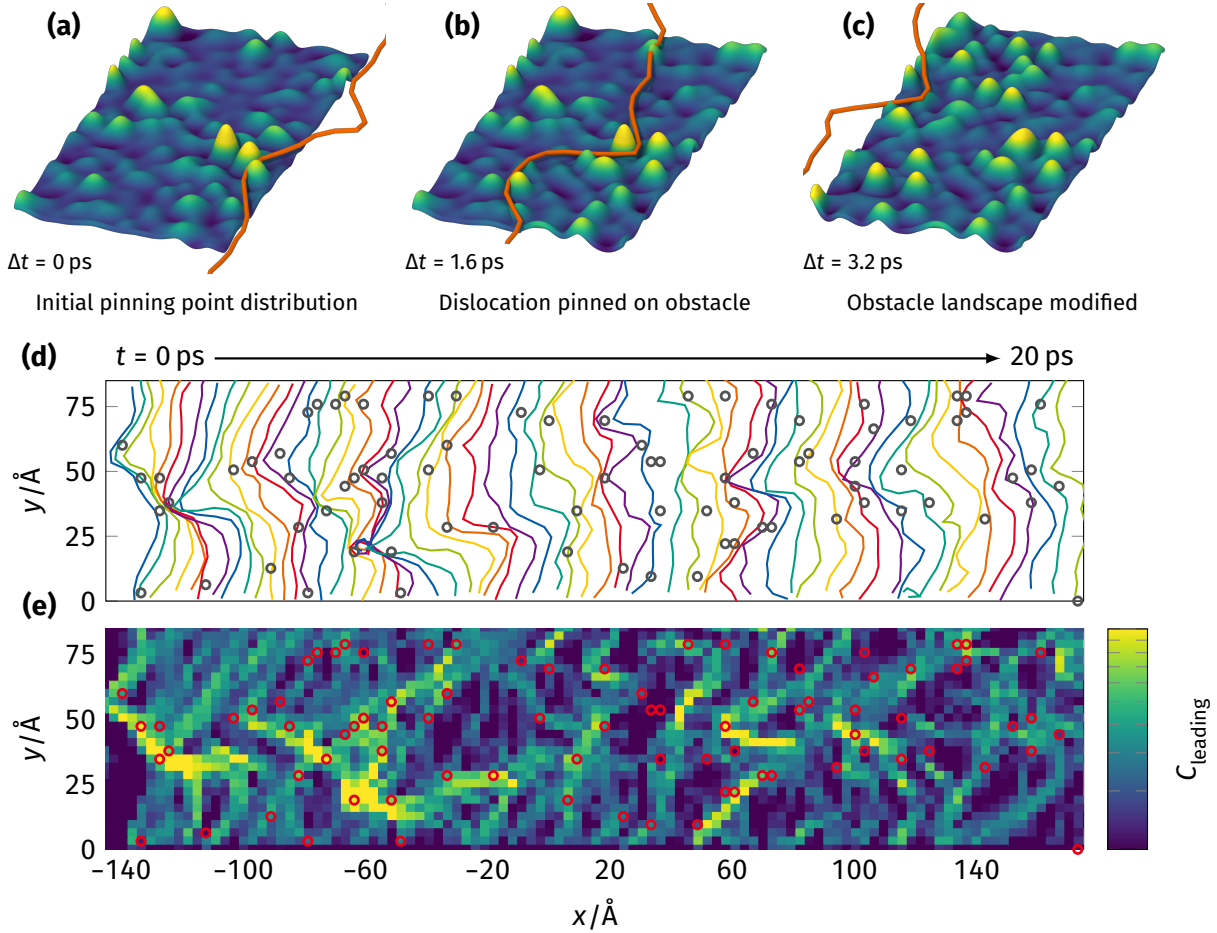


Figure 3: Dislocation moving through its obstacle landscape (a-c) highlighting the pinning of the dislocation line. Spatial and temporal distribution of the dislocation during its glide showing regions of strong pinning (d-e). (a-c) Proposed pinning point landscape around  $x = -120 \text{ \AA}$  showing the initial configuration (a), a bowing out of the dislocation line due to pinning at the highest obstacle (b), and the modified dislocation pinning point landscape after the dislocation rearranged the local chemical environment (c). (d) Position of the leading partial dislocation in 0.25 ps increments over a 20 ps interval. Proposed dislocation pinning points are marked by circles. (e) 2D histogram of the leading partial occupation density  $C_{\text{leading}}$ . Bright yellow spots indicate a long residence time of the dislocation due to local pinning (logarithmic color scale). Red circles highlight proposed pinning points.

therefore suggest stronger pinning sites. Note, that the color scale is logarithmic. Additional red points mark positions of locally increased  $F_{\text{GSF}}$  (sampled on the same grid). These were obtained from local averaging of  $F_{\text{GSF}}$  for the leading partial. While it is difficult to judge the spatial correlation between  $F_{\text{GSF}}$  and  $C_{\text{leading}}$ ; between  $x \approx 140 - 160 \text{ \AA}$ ,  $x \approx 80 - 100 \text{ \AA}$ , or  $x \approx -50 - -20 \text{ \AA}$ , a spatial correspondence of high  $F_{\text{GSF}}$  and long dislocation residence time may be seen. This confirms that the local  $F_{\text{GSF}}$  parameter calculated here is a good descriptor for the local dislocation pinning in the HEA. Supplementary video 2 shows the leading partial dislocation line overlaid on top of the  $F_{\text{GSF}}$  grid where the pinning can be appreciated in motion.

The Pearson product-moment correlation coef-

ficient  $R$  can be used to estimate the correlation between two variables. It becomes 1 for a positive linear correlation and  $-1$  for negative linear correlation [36]. Calculating  $R$  between  $F_{\text{GSF}}$  and  $C$  for the leading and trailing partial dislocations separately gives  $R_{\text{leading}} = 0.14$  and  $R_{\text{trailing}} = 0.16$ , respectively. To give perspective on these numbers, we created many different random arrangements of  $F_{\text{GSF}}$  and found their correlation with the observed  $C$  to be substantially smaller:  $R_{\text{leading}} = R_{\text{trailing}} = 0.00 \pm 0.02$ . Confirming that there is a correlation between the  $F_{\text{GSF}}$  determined for each atom and the dislocation pinning points.

We have found an atomic descriptor of dislocation pinning points in an HEA that does not only describe the observations from our atomistic simulations well but also fits in with expectations from

the established theory of the Peierls model.

To increase solid solution strengthening in alloys a high density of strong dislocation line pinning points is required. Based on our findings, an alloy with a increased number of high  $F_{\text{GSF}}$  lattice sites would be strongest. Using the same routine used for the Cantor alloy in the previous section we tested the hypothesis and created different samples ranging from pure Ni over Ni based binary and ternary alloys up to the HEA and determined the force required for dislocation glide.

Firstly,  $F_{\text{GSF}}$  is determined for a dedicated  $\{111\}$  plane and a dislocation is subsequently inserted. Fig. 4(a) gives the leading partial dislocation's  $F_{\text{GSF}}$  spectra for all species in the sample, while in (b) only the contribution of Co atoms is shown. The binary NiCo alloy is contrasted against NiCoCr and the CoCrFeMnNi HEA. In the NiCo alloy, Ni and Co atoms have very similar  $F_{\text{GSF}}$  values around  $0.2 \text{ eV } \text{\AA}^{-1}$ . If Cr is added to the alloy, the wider range of distinct chemical environments leads to a broadening of the Ni peak, which remains centered around  $0.2 \text{ eV } \text{\AA}^{-1}$ . The Co peak on the other hands not only broadens but also shifts to significantly higher values around  $0.8 \text{ eV } \text{\AA}^{-1}$  while Cr has intermediate  $F_{\text{GSF}}$  values between  $0.4$  and  $0.6 \text{ eV } \text{\AA}^{-1}$ . Further addition of Fe and Mn does not lead to significant shifts in peak positions for any of the 3 elements with Fe and Mn themselves having low  $F_{\text{GSF}}$  around  $0.2 \text{ eV } \text{\AA}^{-1}$ . Their effect is mostly a reduction in the number of high  $F_{\text{GSF}}$  sites due to a reduction in Co and Cr concentration.

From this data we would expect dislocations in NiCo to move the easiest and fastest, while CoCrFeMnNi has intermediate dislocation pinning due it its reduced number of pinning sights compared to NiCoCr where we expect the highest resistance against dislocation glide. We perform two sets of shear simulations on the different samples. First we apply a constantly increasing shear force  $F$  and track the critical force  $F_{\text{crit}}$  required for the leading and trailing partial dislocation to move.  $F_{\text{crit}}$  is chosen as the force required to move each dislocation by  $25 \text{ \AA}$ .

For further analysis the 99.4 percentile of  $F_{\text{GSF}}$  ( $P_{95.4}(F_{\text{GSF}})$ ) is chooses as a measure of the  $F_{\text{GSF}}$  distribution.  $P_{95.4}(F_{\text{GSF}})$  means that 95.4% of the  $F_{\text{GSF}}$  values are lower so it gives a representative number for the upper tail of  $F_{\text{GSF}}$  (see dashed line in (a)). Charting  $F_{\text{crit}}$  against  $P_{95.4}(F_{\text{GSF}})$  for all tested samples reveals a linear correlation (Fig. 4(c)). Showing the initially suggested correlation.

An increased pinning point density should not only influence the the critical force required to initiate dislocation glide but should also reduce its overall mobility. The mobility  $M$  is defined as

$v = M \times F$ , where  $v$  is the dislocation's velocity and  $F$  is the acting force [30]. We apply a constant force of  $F_{\text{crit}}$ . If leading and trailing partial had different  $F_{\text{crit}}$  values, as was the case for samples with a negative stable stacking fault energy (NiCr, NiCoCr, NiCrFe, CoCrFeMnNi), the one for the leading partial was chosen. In those cases, only the mobility of the leading partial was calculated. (d) gives the calculated dislocation mobilities for all samples studied and similar to (c) a correlation between  $P_{95.4}(F_{\text{GSF}})$  and  $M$  can be seen.

While we have shown that the local Peierls energy landscape can be used to describe dislocation pinning in random alloys, the question impact of SRO remains elusive. Here we find that, the  $F_{\text{GSF}}$  spectrum for remains essentially unchanged for four different CoCrFeMnNi SRO samples compared to their random counterpart (see supplementary material). Additionally, we calculate  $F_{\text{crit}}$  and  $M$  for the SRO samples and add it to Fig. 4 (c & d). As expected from our previous analysis, the similarities in  $F_{\text{GSF}}$  between SRO and random samples lead to matching  $F_{\text{crit}}$  and  $M$ . The CoCrFeMnNi samples were produced using Monte-Carlo style optimization algorithm to artificially skew the bond count towards an increased count of A-B bonds. Two samples with varying degrees of instilled SRO are prepared (see supplementary material for the WC SRO analysis of the two different SRO samples). The A-B species, which feature increased bond compared to the random sample are replaced by Co-Cr, which leads to an increase in energy in the sample, thereby being an unfavorable SRO and by Ni-Mn, which is a energetically favorable SRO in these samples.

In summary, we find that the dislocation pinning points identified in the Cantor alloy could also be found in different binary and ternary alloys. The critical force required for a dislocation to move correlates with the amount of high strength pinning points identified from the atomistically resolved GSF curves. Similarly, a greater number of strong pinning sites leads to an overall reduced dislocation mobility.

### 3 Discussion

The stable stacking fault energy for the CoCrFeMnNi alloy calculated from the the interatomic potential are negative indicating that the hexagonal close-packed (HCP) phase is more stable than the FCC phase. This negative stacking fault energy is in line with some density function theory calculations [4, 37], while others report a stable stacking fault energy close to 0 [38] or around  $30 \text{ mJ m}^{-2}$  [39, 40]. Therefore, leading and partial dislocation are not gliding together keeping a constant width. Instead the leading partial starts to

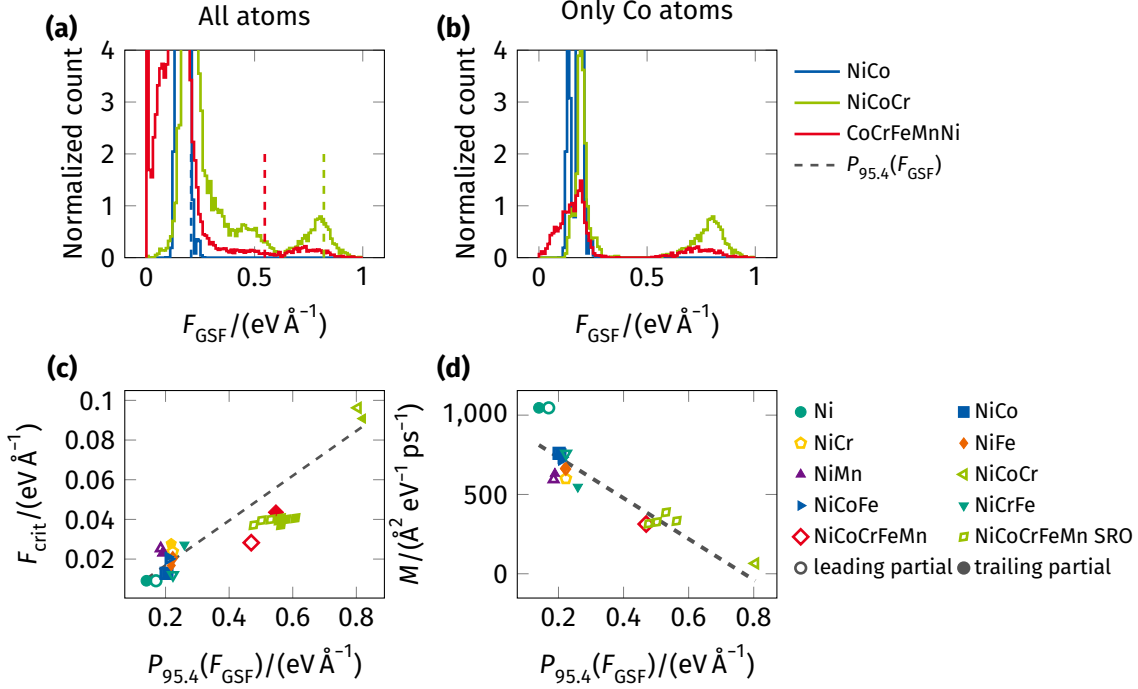


Figure 4: Correlation of the proposed pinning point distribution to the resistance against dislocation glide in several alloys. Distribution of  $F_{\text{GSF}}$  over all atoms in the GSF plane (a) or Co atoms only (b). A dashed line marks the 99.4 percentile of  $F_{\text{GSF}}$  ( $P_{95.4}(F_{\text{GSF}})$ ) threshold for each sample. Comparison of the critical force required for dislocation glide ( $F_{\text{crit}}$ ) (c) and the dislocation mobility  $M$  (d) for all samples against  $P_{95.4}(F_{\text{GSF}})$ . Dashed lines are added as a guide for the eye.

glide while the trailing partial remains in-place as the increasing stacking fault width decreases the overall energy of the crystal. Moreover, the periodic boundary conditions applied to the simulation cell in the glide direction lead to the effect that the leading partial dislocation starts to interact with the stationary trailing partial across the periodic boundary. To reduce the artifacts of the negative stacking fault energy, we only calculated the mobility of the leading partial for these samples. The main conclusion about the nature of the dislocation pinning points in HEAs remains unaffected by the negative stacking fault energy, as we isolated the leading partial dislocation's pinning points and its mobility.

The correlation factor  $R$  calculated here should not be taken as an absolute number attesting to the strength of association.  $R$  can only quantify a linear relationship between two variables. Moreover, other statistical measures need to be met to make quantitative statements based on a given value of  $R$  [36]. Nevertheless, we deem it valuable as a measure to compare the observed spatial distribution of proposed pinning force  $F_{\text{GSF}}$  and the dislocation occupation number  $C$ . Comparing the observed  $R$  to many different random arrangements of  $F_{\text{GSF}}$  showed that the observations cannot be explained by random chance.

Having identified the dislocation pinning points

allowed us to sample their density for different binary and ternary alloys and compare those to the CoCrFeMnNi HEA. Neither Co nor Cr lead to a substantial shift in the  $F_{\text{GSF}}$  distribution when added to Ni. Only the addition of both leads to a pronounced increase in pinning point density and strength. Further addition of Fe and Mn leads to no relevant shift in the  $F_{\text{crit}}$  spectrum and therefore only decreases the pinning point density. This predicted strengthening increase from NiCo and NiCr to NiCoCr from the pinning point analysis is confirmed from our single dislocation shear simulations. These findings are in line with experimental observations, where NiCoCr consistently shows higher hardness [3] and tensile yield strength [41, 42] compared to other alloys from the same family.

We find that the SRO created in the CoCrFeMnNi samples neither influences the SFE landscape nor the forces required for dislocation glide. This is in agreement with a recent study on the CoFeNiTi model HEA [7], where it is found that chemical ordering leads to a strength increase due to the formation of energetically favorable bonds, while simultaneously decreasing the misfit volume of the different elements. Following the solid solution strengthening model this change in the misfit volume leads to a decrease in strength. Pasianot and Farkas find that these two effects compensate

for edge dislocations which offers an explanation for the constant strength observed in Fig 4.

Dislocation waviness observed by Li *et al.* [25] was attributed to differences in the Co-Cr bond count (measured in the form of the Warren-Cowley SRO parameter). This is in agreement with our results where we find the strong interaction of Co and Cr. Note that their results are obtained at higher temperatures of 300 K where thermally activated dislocation glide plays a substantial roll.

To address the open question, whether the single dislocation type studied here, we refer to recent study of pure edge, pure screw and a 60° mixed dislocation in a model FCC HEA. Here it was shown that edge and mixed dislocation are more wavy compared to the screw dislocation. It is found that while the edge dislocation shows the widest partial dislocation separation, the Peierls stress is comparable (100-150 MPa mixed dislocation, 125-150 MPa for edge and screw dislocation) in all three cases [24]. Therefore, the study of an edge dislocation can be seen as representative in the context of our study.

While we have found an atomic scale descriptor to predict possible pinning sites for the dislocation line, this does not result in a full description of solid solution strengthening akin to the works by Varvenne *et al.* [14]. Effects like temperature, dislocation line tension, etc. are neglected in the force – pinning points correlations shown in Fig. 4 (c & d). To extrapolate to a macroscopic yield strength as would be required for a full comparison with published yield strength measurements (*e.g.* Wu *et al.* [41]), the influence of microstructure, impurities in the experimental samples must not be underestimated.

## 4 Conclusion

Having identified the dislocation pinning points answers a long standing question in the HEA community, which has often talked about the existence of dislocation pinning points leading to a wavy or jagged dislocation line, but has so far not been able to identified their origin.

Local pinning of the dislocation line in HEAs is facilitated by a locally increased slope of the general stacking fault curve, which is in agreement with the established Peierls model.

In the interatomic potential model these changes are highly non-linear and the interaction of Co and Cr leads to the highest density of strong dislocation pinning points in the alloy.

The higher density of dislocation pinning points correlates with the critical force required to move an edge dislocation and its mobility over a wide range of equimolar Ni-based alloys with and without short-range order.

## Acknowledgement

The authors would like to acknowledge financial support by the Deutsche Forschungsgemeinschaft (DFG) under grants No. STU 611/2-1 and DE 796/13-1 as part of the SPP 2006. S.L. is funded by Alexander von Humboldt Foundation. Calculations for this research were conducted on the Lichtenberg high performance computer of the TU Darmstadt. The authors gratefully acknowledge the Gauss Centre for Supercomputing e.V. ([www.gauss-centre.eu](http://www.gauss-centre.eu)) for funding this project by providing computing time on the GCS Supercomputer SuperMUC-NG at Leibniz Supercomputing Centre ([www.lrz.de](http://www.lrz.de)).

## References

- [1] Bernd Gludovatz, Anton Hohenwarter, Dhiraj Catoor, Edwin H Chang, Easo P George, and Robert O Ritchie. A fracture-resistant high-entropy alloy for cryogenic applications. *Science*, 345(6201):1153–1158, 2014.
- [2] Zhiming Li, Konda Gokuldoss Pradeep, Yun Deng, Dierk Raabe, and Cemal Cem Tasan. Metastable high-entropy dual-phase alloys overcome the strength–ductility trade-off. *Nature*, 534(7606):227–230, 2016.
- [3] Z. Wu, H. Bei, G.M. Pharr, and E.P. George. Temperature dependence of the mechanical properties of equiatomic solid solution alloys with face-centered cubic crystal structures. *Acta Materialia*, 81:428–441, December 2014.
- [4] Duancheng Ma, Blazej Grabowski, Fritz Körmann, Jörg Neugebauer, and Dierk Raabe. Ab initio thermodynamics of the cocrfemni high entropy alloy: Importance of entropy contributions beyond the configurational one. *Acta Materialia*, 100:90–97, 2015.
- [5] Qing-Jie Li, Howard Sheng, and Evan Ma. Strengthening in multi-principal element alloys with local-chemical-order roughened dislocation pathways. *Nature communications*, 10(1):1–11, 2019.
- [6] Leonie Koch, Fredric Granberg, Tobias Brink, Daniel Utt, Karsten Albe, Flyura Djurabekova, and Kai Nordlund. Local segregation versus irradiation effects in high-entropy alloys: Steady-state conditions in a driven system. *Journal of Applied Physics*, 122(10):105106, September 2017.
- [7] E. Antillon, C. Woodward, S.I. Rao, B. Akdim, and T.A. Parthasarathy. Chemical short range order strengthening in a model FCC high entropy alloy. *Acta Materialia*, 190:29–42, May 2020.

- [8] Frederik Otto, Ying Yang, Hongbin Bei, and Easo P George. Relative effects of enthalpy and entropy on the phase stability of equiatomic high-entropy alloys. *Acta Materialia*, 61(7):2628–2638, 2013.
- [9] EJ Pickering, R Muñoz-Moreno, HJ Stone, and NG Jones. Precipitation in the equiatomic high-entropy alloy crmnfeconi. *Scripta Materialia*, 113:106–109, 2016.
- [10] Jun Ding, Qin Yu, Mark Asta, and Robert O Ritchie. Tunable stacking fault energies by tailoring local chemical order in crconi medium-entropy alloys. *Proceedings of the National Academy of Sciences*, 115(36):8919–8924, 2018.
- [11] Binglun Yin, Shuhei Yoshida, Nobuhiro Tsuji, and W. A. Curtin. Yield strength and misfit volumes of NiCoCr and implications for short-range-order. *Nature Communications*, 11(1):2507, December 2020.
- [12] Ruopeng Zhang, Shiteng Zhao, Jun Ding, Yan Chong, Tao Jia, Colin Ophus, Mark Asta, Robert O Ritchie, and Andrew M Minor. Short-range order and its impact on the crconi medium-entropy alloy. *Nature*, 581(7808):283–287, 2020.
- [13] W.G. Nöhring and W.A. Curtin. Design using randomness: A new dimension for metallurgy. *Scripta Materialia*, 187:210–215, October 2020.
- [14] Céline Varvenne, Aitor Luque, and William A. Curtin. Theory of strengthening in fcc high entropy alloys. *Acta Materialia*, 118:164–176, October 2016.
- [15] MJ Yao, Konda Gokuldoss Pradeep, Cemal Cem Tasan, and Dierk Raabe. A novel, single phase, non-equiatomic femnnicocr high-entropy alloy with exceptional phase stability and tensile ductility. *Scripta Materialia*, 72:5–8, 2014.
- [16] Norihiko L Okamoto, Shu Fujimoto, Yuki Kambara, Marino Kawamura, Zhenghao MT Chen, Hirotaka Matsunoshita, Katsushi Tanaka, Haruyuki Inui, and Easo P George. Size effect, critical resolved shear stress, stacking fault energy, and solid solution strengthening in the crmnfeconi high-entropy alloy. *Scientific reports*, 6:35863, 2016.
- [17] Subin Lee, María Jazmin Duarte, Michael Feuerbacher, Rafael Soler, Christoph Kirchlechner, Christian H Liebscher, Sang Ho Oh, and Gerhard Dehm. Dislocation plasticity in fecocrmnni high-entropy alloy: quantitative insights from in situ transmission electron microscopy deformation. *Materials Research Letters*, 8(6):216–224, 2020.
- [18] FX Zhang, Shijun Zhao, Ke Jin, H Xue, G Velisa, H Bei, R Huang, JYP Ko, DC Pagan, JC Neufeind, et al. Local structure and short-range order in a nicocr solid solution alloy. *Physical review letters*, 118(20):205501, 2017.
- [19] Frederik Otto, A Dlouhý, Ch Somsen, Hongbin Bei, G Eggeler, and Easo P George. The influences of temperature and microstructure on the tensile properties of a cocrfemnni high-entropy alloy. *Acta Materialia*, 61(15):5743–5755, 2013.
- [20] Evan Ma. Unusual dislocation behavior in high-entropy alloys. *Scripta Materialia*, 181:127–133, May 2020.
- [21] T.M. Smith, M.S. Hooshmand, B.D. Esser, F. Otto, D.W. McComb, E.P. George, M. Ghazisaeidi, and M.J. Mills. Atomic-scale characterization and modeling of 60 dislocations in a high-entropy alloy. *Acta Materialia*, 110:352–363, May 2016.
- [22] G Laplanche, A Kostka, OM Horst, G Eggeler, and EP George. Microstructure evolution and critical stress for twinning in the crmnfeconi high-entropy alloy. *Acta Materialia*, 118:152–163, 2016.
- [23] S.I. Rao, C. Woodward, T.A. Parthasarathy, and O. Senkov. Atomistic simulations of dislocation behavior in a model FCC multicomponent concentrated solid solution alloy. *Acta Materialia*, 134:188–194, August 2017.
- [24] Roberto Pasianot and Diana Farkas. Atomistic modeling of dislocations in a random quinary high-entropy alloy. *Computational Materials Science*, 173:109366, February 2020.
- [25] Qing-Jie Li, Howard Sheng, and Evan Ma. Strengthening in multi-principal element alloys with local-chemical-order roughened dislocation pathways. *Nature Communications*, 10(1):3563, December 2019.
- [26] Daniel Kiener, Christian Motz, Martin Rester, Monika Jenko, and Gerhard Dehm. Fib damage of cu and possible consequences for miniaturized mechanical tests. *Materials Science and Engineering: A*, 459(1-2):262–272, 2007.
- [27] Joachim Mayer, Lucille A Giannuzzi, Takeo Kamino, and Joseph Michael. Tem sample preparation and fib-induced damage. *MRS bulletin*, 32(5):400–407, 2007.

- [28] S. Plimpton. Fast parallel algorithms for short-range molecular dynamics. Technical Report SAND-91-1144, 10176421, May 1993.
- [29] Won-Mi Choi, Yong Hee Jo, Seok Su Sohn, Sunghak Lee, and Byeong-Joo Lee. Understanding the physical metallurgy of the CoCrFeMnNi high-entropy alloy: An atomistic simulation study. *npj Computational Materials*, 4(1):1, December 2018.
- [30] John Price Hirth and Jens Lothe. *Theory of Dislocations*. Wiley, New York, 2nd ed edition, 1982.
- [31] Vasily V. Bulatov and Wei Cai. *Computer Simulations of Dislocations*. Number 3 in Oxford Series on Materials Modelling. Oxford Univ. Press, Oxford, reprinted edition, 2008.
- [32] V. Vitek. Intrinsic stacking faults in body-centred cubic crystals. *Philosophical Magazine*, 18(154):773–786, October 1968.
- [33] V. Vitek. Core structure of screw dislocations in body-centred cubic metals: Relation to symmetry and interatomic bonding. *Philosophical Magazine*, 84(3-5):415–428, January 2004.
- [34] Gang Lu, Nicholas Kioussis, Vasily V. Bulatov, and Efthimios Kaxiras. Generalized-stacking-fault energy surface and dislocation properties of aluminum. *Physical Review B*, 62(5):3099–3108, August 2000.
- [35] Hyun Oh, Duancheng Ma, Gerard Leyson, Blazej Grabowski, Eun Park, Fritz Körmann, and Dierk Raabe. Lattice Distortions in the FeCoNiCrMn High Entropy Alloy Studied by Theory and Experiment. *Entropy*, 18(9):321, September 2016.
- [36] Patrick Schober, Christa Boer, and Lothar A. Schwarte. Correlation Coefficients: Appropriate Use and Interpretation. *Anesthesia & Analgesia*, 126(5):1763–1768, May 2018.
- [37] Shijun Zhao, G. Malcolm Stocks, and Yanwen Zhang. Stacking fault energies of face-centered cubic concentrated solid solution alloys. *Acta Materialia*, 134:334–345, August 2017.
- [38] Shuo Huang, Wei Li, Song Lu, Fuyang Tian, Jiang Shen, Erik Holmström, and Levente Vitos. Temperature dependent stacking fault energy of FeCrCoNiMn high entropy alloy. *Scripta Materialia*, 108:44–47, November 2015.
- [39] A. J. Zaddach, C. Niu, C. C. Koch, and D. L. Irving. Mechanical Properties and Stacking Fault Energies of NiFeCrCoMn High-Entropy Alloy. *JOM*, 65(12):1780–1789, December 2013.
- [40] M. Beyramali Kiviy and M. Asle Zaeem. Generalized stacking fault energies, ductilities, and twinnabilities of CoCrFeNi-based face-centered cubic high entropy alloys. *Scripta Materialia*, 139:83–86, October 2017.
- [41] Z. Wu, H. Bei, F. Otto, G.M. Pharr, and E.P. George. Recovery, recrystallization, grain growth and phase stability of a family of FCC-structured multi-component equiatomic solid solution alloys. *Intermetallics*, 46:131–140, March 2014.
- [42] C.E. Slone, J. Miao, E.P. George, and M.J. Mills. Achieving ultra-high strength and ductility in equiatomic CrCoNi with partially recrystallized microstructures. *Acta Materialia*, 165:496–507, February 2019.
- [43] RD Field and PA Papin. Location specific in situ tem straining specimens made using fib. *Ultramicroscopy*, 102(1):23–26, 2004.
- [44] Pierre Hirel. Atomsk: A tool for manipulating and converting atomic data files. *Computer Physics Communications*, 197:212–219, December 2015.
- [45] Alexander Stukowski, Vasily V Bulatov, and Athanasios Arsenlis. Automated identification and indexing of dislocations in crystal interfaces. *Modelling and Simulation in Materials Science and Engineering*, 20(8):085007, December 2012.
- [46] Alexander Stukowski. Visualization and analysis of atomistic simulation data with OVITO—the Open Visualization Tool. *Modelling and Simulation in Materials Science and Engineering*, 18(1):015012, January 2010.

## 5 Methodology

### 5.1 Materials preparation

A single crystal CoCrFeMnNi HEA was produced by using Czochralski method from an equiatomic melt of high-purity elements. The composition of Fe, Co, Cr, Mn and Ni is 24, 24, 20, 12, 20 at.%, respectively, measured by both STEM-EDS and atom probe tomography (APT) [17]. In-situ TEM straining samples were prepared by focused ion beam (FIB) site specific lift-out method [43] which utilize a 30 and 5 kV Ga ion beam (JIB-4610F, JEOL). A thin lamella with a size of  $10 \times 5 \times 0.1 \mu\text{m}$  was glued on custom made Cu grid by Pt deposition [17].

## 5.2 Transmission electron microscopy

In-situ tensile straining tests were carried out in an aberration-corrected TEM operated at 300 kV (JEM-ARM300CF, JEOL) equipped with a straining holder (Model 654, Gatan). In-situ TEM movies were recorded with a high-speed camera at frame rate of 50 frames per second and 2k resolution (Oneview, Gatan). The displacement of the whole sample grid was controlled by a step motor whose resolution was 1  $\mu\text{m}$ . The loading was interrupted intermittently to stabilize the stage and observe dislocation glide motion. No quantitative load-displacement data were obtained during the testing. The contrast of dislocations in TEM images and videos are enhanced by image processing. Firstly, the background noise from the FIB damage is removed by using direct subtraction of the last frame after aligning all frames using cross correlation method. Then, Gaussian filter is used to blur the remaining noise. To extract dislocation positions shown in Fig. 1 (d), ridge detection filter is used after applying additional Gaussian filter.

## 5.3 Simulation

Computer simulations are performed using LAMMPS [28]. All atomic interactions are based on the interatomic modified embedded atom method interatomic potential parametrized by Choi *et al.* [29]. The atoms were placed randomly on FCC lattice sites to create ideally random solid solution alloys.

A large sample measuring  $177 \times 499 \times 270 \text{ \AA}^3$  with periodic boundary conditions along  $x$  and  $y$  and an open surface along  $z$  is used. A notch is cut into the surface and it is subjected to uniaxial strain in the  $y$  direction at 300 K. The applied strain rate is equal to  $10^8 \text{ s}^{-1}$  and the final strain is set to 10 %.

The generalized stacking fault energy surface is calculated for a singlecrystalline FCC sample oriented  $x = [1\bar{1}0]$ ,  $y = [11\bar{2}]$ , and  $z = [111]$  measuring  $510 \times 89 \times 123 \text{ \AA}^3$ . Here periodic boundary conditions were employed in  $x$  and  $y$  direction keeping an open surface along  $z$ . The GSF energy surface is obtained from rigid displacement of the upper half of the crystal against the lower half along the  $x$  and  $y$  direction. Due the strong variations in equilibrium bond length in the HEA, the atoms were kept fixed on their ideal FCC lattice sites during the subsequent energy minimization. Both crystallites were allowed to rigidly shift along the  $z$  direction to avoid overlapping atoms in the GSF plane.

The samples for which the GSF surface were taken and an additional half plane was inserted in the  $x$  direction to create an edge dislocation with its glide plane identical to the GSF plane. All

subsequent simulations were performed at 2 K in the micro-canonical (NVE) ensemble. A 4  $\text{\AA}$  layer at the open surfaces was thermostatted using a Langevin thermostat to retain constant temperature.

For the initial simulations on the CoCrFeMnNi HEA a constant shear force of  $0.052 \text{ eV \AA}^{-1} \text{ at}^{-1}$  was applied to the surface atoms facilitating dislocation migration. For the determination of the critical force  $F_{\text{crit}}$  required for dislocation migration a constantly increasing shear force ( $1.04 \text{ meV \AA}^{-1} \text{ at}^{-1} \text{ ps}^{-1}$ ) was applied to the surface atoms until the dislocation started to glide. To measure the dislocation mobility, the force was ramped from 0 to  $F_{\text{crit}}$  which was held to determine the dislocation velocity under constant force.

All samples were built using ATOMSK [44]. The dislocation lines are determined using the dislocation extraction algorithm [45] implemented in OVITO [46].

## Supplementary Material

Video 1: Video 1 shows the glide of a series of partial dislocations during in-situ TEM straining. To increase the signal-to-noise ratio by removing the background features, the last frame is subtracted from all other frames after aligning the frame by using cross-correlation drift correction. The dark bands in the video are stacking faults of which left and right ends are trailing and leading partial dislocations, respectively.

Video 2: Video 2 shows the leading partial dislocation under applied constant shear load migrating through the chemically complex HEA matrix. The underlying grid shows the local average of  $F_{\text{crit}}$  on a  $3 \times 3 \text{ \AA}^2$  grid.

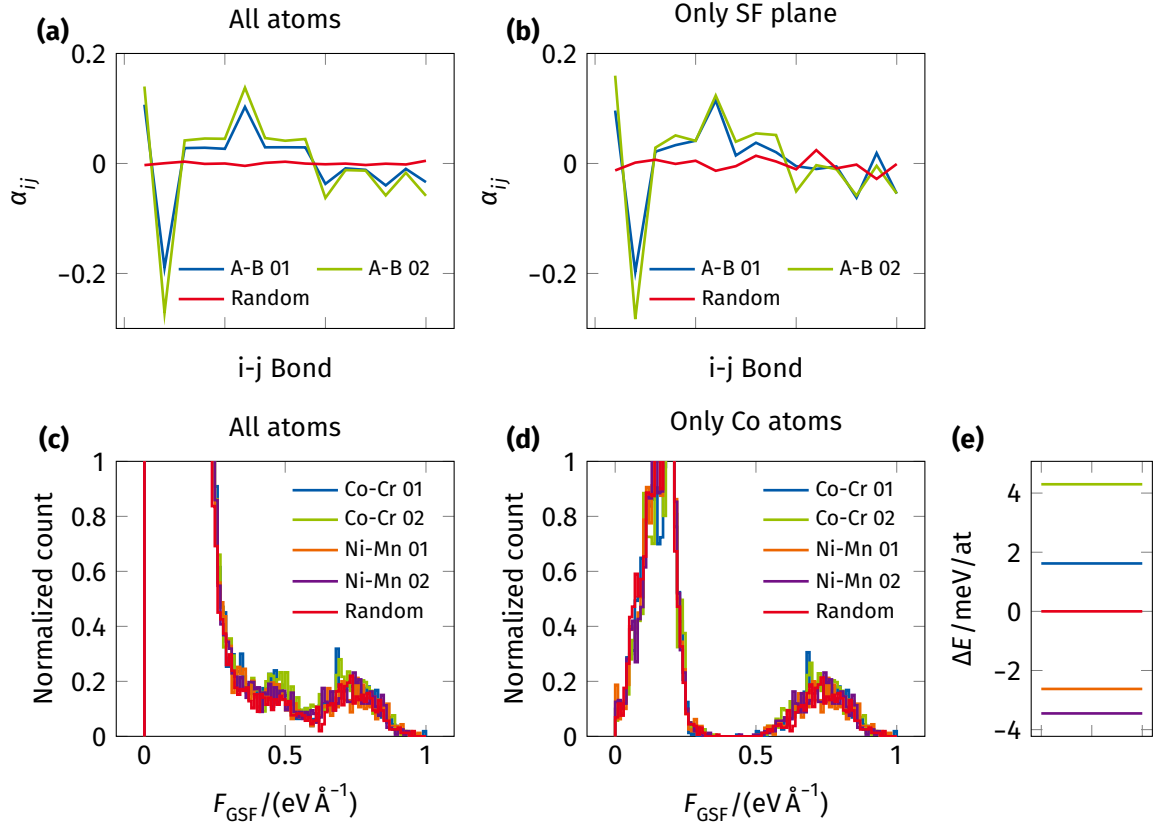


Figure 5: Warren Cowley short range order (SRO) parameter  $\alpha_{ij}$  citeCowley1950 for the random CoCrFeMnNi sample compared to the two artificially created (A-B 01 & A-B 02). (a) shows the average over the whole samples, while in (b) only the average over the stacking fault plane is taken. Both SRO samples show one bond being clearly favored, while all other bond fractions are modified by approximately the same amount compared to the perfectly random sample. In the following this favored A-B pair is once replaced by Co-Cr and once by Ni-Mn. (c & d) distribution of  $F_{\text{crit}}$  for the random CoCrFeMnNi sample compared to the different SRO samples (see also Fig. 4). The spectrum is not significantly modified by the addition of SRO. (e) Energy difference per atom between the different SRO samples compared to the random sample. Preference of Co-Cr is energetically unfavorable while Ni-Mn leads to an overall energy decrease.